Photoelectron angular distributions from polarized Ne* atoms near threshold

P. O'Keeffe and P. Bolognesi
National Research Council–Institute of Inorganic Methodologies and Plasmas, Area della Ricerca di Roma 1, I-00016 Monterotondo Scalo, Italy

A. Mihelič
Jožef Stefan Institute, Jamova cesta 39, SI-1000 Ljubljana, Slovenia

A. Moise, R. Richter, G. Cautero, L. Stebel, and R. Sergo
Sincrotrone Trieste SCpA, Area Science Park, I-34149 Basovizza (Trieste), Italy

L. Pravica
The University of Western Australia, 35 Stirling Highway, Crawley, Western Australia

E. Ovcharenko
Institute of Electron Physics, 88017 Uzhgorod, Ukraine

P. Decleva
Dipartimento di Scienze Chimiche, Universitá di Trieste, I-34127 Trieste, Italy

L. Avaldi
National Research Council–Institute of Inorganic Methodologies and Plasmas, Area della Ricerca di Roma 1, I-00016 Monterotondo Scalo, Italy

(Received 8 September 2010; published 29 November 2010)

Photoelectron distributions of the polarized $2p^5 3d$ Rydberg states of neon have been studied with a newly built velocity map imaging analyzer. The atoms were polarized by absorption of synchrotron radiation and ionized by an infrared laser. The asymmetry parameters β_2 and β_4 characterizing two-photon resonant ionization have been extracted from the measured images and compared with the results of a quantum defect treatment. To achieve a good theoretical description of the data, it is necessary to take into account the dependence of the dipole transition matrix elements and phases of the partial waves on the angular momentum quantum numbers pertaining to various continuum channels.

DOI: 10.1103/PhysRevA.82.052522 PACS number(s): 31.50.Df, 32.80.Rm, 31.15.A−

I. INTRODUCTION

Photoionization of polarized atoms is a useful tool for probing detailed aspects of the photoionization process. This point is underlined in the work of Klar and Kleinpoppen [1], who pointed out that the measurement of the angular distribution of photoelectrons emitted from polarized atoms can provide the "complete" information on the ionization process. Here, complete information signifies the measurement of a sufficient number of experimental observables such that all other unmeasured observables can be predicted. Obviously, any experiment is "complete" only up to the level of approximation of the theoretical model used to describe the process.

A possible way of preparing a polarized atomic target is by photoexcitation with polarized light. The resulting polarized atoms are then photoionized by another polarized light source. One of the most important experimental methods for these types of measurements involves the combination of synchrotron and laser radiation sources. For extensive reviews of this class of experiments see Refs. [2,3], which include a historical evolution of these experiments with increasing sophistication of synchrotron sources and detectors over the last three decades. Either source can be used to photo-prepare a polarized ensemble of atoms, which can then be ionized by the second radiation source.

In the case where visible radiation is used in the first step, the most common type of experiment is to excite alkali or alkali earth metals with the laser, and to ionize the resulting excited atom with relatively highly energetic synchrotron radiation (for recent examples see Refs. [4–7] and the references therein). This allows the inner-shell ionization of the atoms to be studied by analyzing the kinetic energy of the electrons emitted. The common methods used in this case are the measurement of the linear alignment dichroism, linear magnetic dichroism in the angular distribution, and circular magnetic dichroism, in which the intensity is measured as a function of the relative polarization of the two light sources.

However, experiments in which the synchrotron is used as a pump and the laser radiation is used as a probe (e.g., Refs. [8–12]) are more relevant to the present work as the atomic targets in this work are rare gas atoms, which do not have low-lying excited states accessible to excitation by visible laser light. Therefore, in this case, it is the synchrotron radiation which is used to excite the atom into a Rydberg state, and subsequently the atom is ionized by the laser light.

In most experiments using this scheme, double-resonance excitations have been studied, in which the laser induces a second resonant transition to autoionizing states between the spin-orbit split ionization thresholds of the rare gas atom. These studies concentrated either on the spectroscopy of the two-photon accessible Rydberg states [8,11,12] (not accessible by single-photon excitation from the ground state due to the selection rules), on the line shapes of these resonances [10], or on the determination of the partial cross sections using the variable polarization of both sources [9]. In these cases, the total ion yield is measured as the experiments are targeted at the measurement of the integral cross sections. Fewer experiments of this type have been dedicated to the detection of electrons and their angular distributions [13]. This may be partially explained by the fact that the photons of the visible laser light used in these studies usually have energies lower than 3 eV, resulting in photoelectrons with a relatively low kinetic energy, while most electron spectrometers used at synchrotron sources are optimized for higher kinetic energy electrons. Nonetheless, some studies exist in which electrons were detected, a notable example of which is the work of Mitsuke *et al.* [13]. They measured the angular distributions of photoelectrons emitted from polarized Rydberg states of Ar for a fixed laser wavelength. As will be explained in the text, due to a difference in the geometry of the experimental technique used in that study with respect to the present work, more experimental parameters describing the photoionization process can be extracted from the photoelectron angular distributions (PADs) presented here.

In order to complete the background on this type of photoionization experiments, it is also necessary to mention experiments performed with high-order harmonic generation (HHG) sources using femtosecond lasers to produce the vacuum ultraviolet (VUV) light to excite the Rydberg atoms [14] and the two-photon two-laser ionization of metastable excited rare gas atoms generated in dc discharges [15–17]. The first of these sources have recently been employed to investigate the PADs resulting from the photoionization of the aligned He $1s3p$ and $1s4p$ $^1P_1$ atoms [14]. Indeed, this work, which employed the same experimental method and geometry as is used in the present case for the measurement of the PADs, showed the potential of the method to extract detailed information on the photoionization process and as a result provided complete information on the photoionization process allowing theory to be tested fully [14]. However, due to the limited tunability of the HHG sources, this method is not applicable to the photoionization of a wide range of rare gas Rydberg states. The second method, on the other hand, forms the basis of a series of papers by Hotop and coworkers [15–17], in which a beam of either metastable Ne ($2p^5 3s$ $^3P_2$) or Ar ($3p^5 4s$ $^3P_2$) atoms produced in a dc discharge source are excited by the first laser to form a polarized sample of Ne ($2p^5 3p$ $^3D_3$) or Ar ($3p^5 4p$ $^3D_3$) atoms. These polarized atoms are then photoionized by the second laser. This far reaching series of papers provided deep insights into the photoionization process in rare gas atoms.

From a theoretical point of view, the work of Baier *et al.* [18] and the work of Cherepkov *et al.* [19] provide a solid basis for the theoretical description of the angular distributions of electrons emitted in the photoionization of polarized atoms. These models (or more recent variants thereof; cf. Ref. [20]) have provided the theoretical basis for the description of many of the experimental results described above.

In this paper, we concentrate on the use of the velocity map imaging (VMI) technique to measure the PADs resulting from the photoionization of the aligned Ne $2p^5 3d$ Rydberg states converging to the $2p_{3/2}$ and $2p_{1/2}$ ionization thresholds. To our knowledge, it is the first time that this experimental technique has been applied to synchrotron plus laser pump-probe experiments. It will be shown here that there are advantages of its use over methods traditionally used at synchrotron sources. In particular, it will be shown that the experimental geometry of velocity map imaging provides access to more experimentally measurable parameters than other fixed geometries (this point will be fully discussed in Sec. IV C). The results will be compared with the angular distributions calculated using the quantum defect theory. Furthermore, the standard approximation of assuming that the single-electron dipole matrix elements and phase shifts only depend on the orbital angular momentum of the outgoing electron waves will be tested.

II. EXPERIMENTAL SETUP AND DATA ANALYSIS

The experiments described in this work have been performed at the branch line of the gas phase photoemission beam line at the Italian synchrotron radiation source Elettra, Trieste. A schematic view of the experimental setup is shown in Fig. 1. The general layout and performance of the beam line is described elsewhere [21]. We will therefore concentrate principally on a description of the additional apparatus necessary for the synchrotron plus laser velocity map imaging experiments.

The details of the laser system in use on the beam line have also been published previously [12], and only a

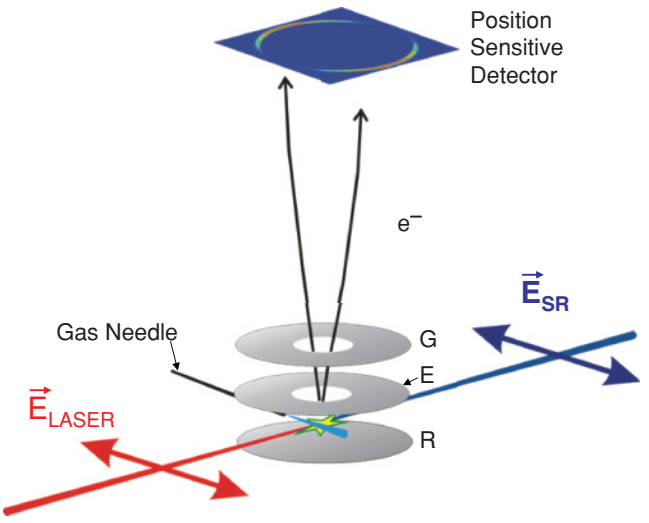

FIG. 1. (Color online) Schematic view of the geometry of the experimental setup. The polarization of the synchrotron light and the polarization of the Ti:sapphire laser (double arrows) are parallel to each other and the beams are counterpropagating. The electrodes are labeled as follows: R, repeller; E, extractor; and G, ground. Details of the setup can be found in the text.

brief description is given here. The laser employed is a commercial mode lockable Ti:sapphire oscillator (Tsunami, Spectra Physics) tunable in the range of 670–1000 nm. In the experiments reported here, the laser was used in a continuous wave (cw) mode due to the relatively long lifetimes of the intermediate states. In the multibunch mode used during these experiments, the time between electron bunches in the storage ring was 2 ns (this corresponds to the synchrotron radio frequency of 500 MHz), and therefore, as the intermediate states pumped by the synchrotron have a much longer lifetime [22,23], no gain is achieved on passing from the cw to the pulsed mode of the laser.

Both light sources are focused to the interaction region of a newly built VMI spectrometer. The electrode dimensions and spacings are similar to those of the VMI spectrometer reported in Ref. [24], while the distance from the interaction region to the position sensitive detector (PSD) is 210 mm. The focal region of the synchrotron source in the interaction zone is a circle with the diameter of about 300 μm, while the laser is focused with a 50-cm focal-length lens, and thus we estimate its diameter to be approximately 250 μm in the interaction region. The neon gas is introduced into the interaction region by an effusive jet at 90° with respect to the propagation direction of the two light sources formed by a brass needle of internal diameter of 250 μm (Fig. 1).

The PSD used in the VMI apparatus has been designed and built by the Instrumentation and Detectors Laboratory at Sincrotrone Trieste. Its details have been published previously [25]. Briefly, the detector is based on the use of two delay-line anodes placed behind two microchannel plates and has a spatial resolution of approximately 70 μm. Furthermore, it has an active area of dimensions 30 × 30 mm. A full description of the entire VMI apparatus used in these experiments will be given in a forthcoming publication [26].

In the experiment presented here, the synchrotron radiation was tuned to excite either the Ne $2p^5(^2P_{3/2})\,3d[3/2]_1$ or the Ne $2p^5(^2P_{1/2})\,3d[3/2]_1$ state from the ground state with photon energies equal to 20.0404 or 20.1395 eV, respectively. The jK-coupling notation $[K]_J$ (see Ref. [27]) is used here to describe the coupling of the $3d$ electron to the ionic core. Linearly polarized laser light was then used to ionize these states with a number of different wavelengths, thus probing different parts of the continuum. It was also possible to scan the laser wavelength while monitoring either the total electron or total ion yield and verifying that the photoionization takes place into a flat (nonresonant) continuum [12]. The bandwidths of the synchrotron and the Ti:sapphire laser were narrow compared to the energy splitting of the $2p^5 3d$ ($J = 1$) intermediate states and the energy differences between the resonance states in the autoionization region (i.e., the energy region between the $2p_{3/2}$ and the $2p_{1/2}$ ionization thresholds). We were therefore able to choose the energy of synchrotron radiation to selectively excite the chosen intermediate state, and the energy of the laser in such a way to avoid double-resonance excitation (and subsequent ionization) in the autoionization region. For each laser wavelength, an image was acquired for about 1 h. A background image was also taken in which only the synchrotron light was allowed to pass through the interaction region.

The raw images were then inverted using the pBasex routine introduced by Garcia *et al.* [28]. The pBasex method works by reconstructing the original three-dimensional (3D) distributions of the emitted electrons by fitting a set of basis functions of known inverse Abel integral to the two-dimensional (2D) projected image.

The two-photon PADs for photoionization using two linearly polarized photons with their electric field vectors parallel to each other are completely described by the asymmetry parameters β_2 and β_4 defined through [29]

$$\frac{d\sigma}{d\Omega} = \frac{\sigma}{4\pi}[1 + \beta_2 P_2(\cos\theta) + \beta_4 P_4(\cos\theta)], \qquad (1)$$

where $d\sigma/d\Omega$ is the differential photoionization cross section, σ is the total (angle-integrated) cross section, and θ is the angle between the polarization of the incident photons and the direction of the ejected electron. It has been assumed in Eq. (1) that the dipole approximation is valid: higher-order transition amplitudes (quadrupole, octupole, etc.) are assumed to be negligible in comparison with the dipole amplitude. The asymmetry parameters β_2 and β_4 are extracted from the images by the previously mentioned fitting procedure.

III. THEORETICAL DESCRIPTION OF THE PHOTOIONIZATION OF POLARIZED ATOMS

The intermediate states we consider in the present experiment are as follows: (1) Ne $2p^5(^2P_{1/2})3d[3/2]_1$ and (2) Ne $2p^5(^2P_{3/2})3d[3/2]_1$. These states are each described by a single configuration state function (weight $\geqslant 95\%$) if the jK-coupling scheme is used. As is customary, we indicate the $J_c = 1/2$ core by a prime, and thus the two processes investigated in this work can be described as

$$\text{Ne}\, 2p^6 \overset{\hbar\omega_S}{\rightarrow} \text{Ne}\, 2p^5 3d'[3/2]_1 \overset{\hbar\omega_L}{\rightarrow} \text{Ne}^+ 2p^5(^2P_{1/2}) + e^-, \qquad (2)$$

and

$$\text{Ne}\, 2p^6 \overset{\hbar\omega_S}{\rightarrow} \text{Ne}\, 2p^5 3d[3/2]_1 \overset{\hbar\omega_L}{\rightarrow} \text{Ne}^+ 2p^5(^2P_{3/2}) + e^-. \qquad (3)$$

The energies of the synchrotron and laser photons are denoted with $\hbar\omega_S$ and $\hbar\omega_L$, respectively.

The aim of a theoretical description is to derive a relationship between the measurable asymmetry parameters describing the angular distribution and the radial matrix elements and phases of the outgoing electron partial waves. This goal can be achieved in two ways. The first method is to calculate the radial matrix elements and phase differences and then to calculate β_2 and β_4 directly. In this case there is no need to reduce the number of parameters describing the process to a number equal to or less than the experimental parameters, and therefore fewer assumptions need to be made in describing the process. The second method, on the other hand, is to make a sufficient number of approximations, such that the number of experimental parameters completely describes the photoionization process, and then deduce directly the quantum mechanical quantities from the experimental data. In this work, we will adopt both approaches. The theoretical framework for both methods is outlined in the following.

A. Quantum defect treatment

In this section, we derive the expressions for the asymmetry parameters in terms of the dipole transition amplitudes and

phase differences associated with various continuum channels. As mentioned earlier, the energy $\hbar\omega_S$ is selected to excite a given intermediate state, while the energy $\hbar\omega_L$ is chosen in such a way as to avoid double-resonance excitation in the autoionization region. This allows a rather simple theoretical treatment in which the interaction between the channels with different angular momenta of the atomic core J_c can be neglected. Note that unlike the d resonances accessible by one-photon excitation [23], the p and f resonance states are narrow [12]. Consequently, the photon energies can be chosen not to lie close to or on-resonance with the resonances in the autoionization region ($J_c = 1/2$ discrete states embedded in the $J_c = 3/2$ continuum), and the bound-continuum configuration interaction is not considered.

In this case, the final state is described by the propagation vector $\boldsymbol{k}$, angular momentum of the atomic core J_c and its projection M_c, and the projection m_s of the spin $s = 1/2$ of the photoelectron (Hartree atomic units are used):

$$|\boldsymbol{k}; J_c M_c m_s\rangle = \sum_{l,m_l}\sum_{K,Q}\sum_{J,M} i^l e^{-i\sigma_l} e^{-i\pi\mu_\gamma} k^{-1/2} Y^*_{l,m_l}(\hat{\boldsymbol{k}}) \times (J_c M_c l m_l | K Q)(K Q s m_s | J M)|\epsilon; \gamma M\rangle. \quad (4)$$

In Eq. (4), γ is used to denote the quantum numbers J_c, l, K, and J, while σ_l and μ_γ are the Coulomb phase shift of the partial wave with orbital angular momentum l and the quantum defect associated with the continuum electron, respectively. The kinetic energy of the ejected electron is $\epsilon = k^2/2$. Note that the decomposition used in Eq. (4) corresponds to jK coupling ($\boldsymbol{K} = \boldsymbol{J}_c + \boldsymbol{l}$, $\boldsymbol{J} = \boldsymbol{K} + \boldsymbol{s}$), which is exact when the spin-orbit interaction between the orbital angular momentum and spin of the continuum electron is negligibly small in comparison with the spin-orbit interaction of the core ($2p$) electrons. We are going to discuss this choice in the following.

The generalized differential two-photon ionization cross section is written as [30]

$$\frac{d\sigma^{(2)}}{d\Omega} = 2\pi(2\pi\alpha)^2\omega_S\omega_L k \sum_{M_c,m_s} |T^{(2)}(\boldsymbol{k})|^2, \quad (5)$$

where $T^{(2)}(\boldsymbol{k}) = \langle \boldsymbol{k}; J_c M_c m_s | D^{(2)} | i\rangle$ is a two-photon transition amplitude connecting the ground state $|i\rangle$ and the final continuum state. Since the energy of the synchrotron photons ω_S is chosen to lie on resonance with the intermediate states in both cases considered here, the two-photon transition amplitude is well approximated by taking into account a single state in the sum over the intermediate states,

$$\sum_{M_c,m_s} |T^{(2)}|^2 \approx \sum_{M_c,m_s} \left| \frac{\langle \boldsymbol{k}; J_c M_c m_s | D | \nu\rangle\langle \nu | D | i\rangle}{E_i + \omega_S - E_\nu + i\Gamma_\nu/2} \right|^2 = \frac{4|\langle \nu | D | i\rangle|^2}{\Gamma_\nu^2} \sum_{M_c,m_s} |\langle \boldsymbol{k}; J_c M_c m_s | D | \nu\rangle|^2, \quad (6)$$

with $\omega_S = E_\nu - E_i$ and $\epsilon = E_i + \omega_S + \omega_L - I_{J_c}$. The energy and the radiative width of the $2p^5 3d$ or $2p^5 3d'$ intermediate state $|\nu\rangle$ are denoted by E_ν and Γ_ν, respectively, and $D = \hat{\boldsymbol{e}} \cdot (\boldsymbol{r}_1 + \boldsymbol{r}_2 + \cdots)$ is the dipole transition operator (with polarization vector $\hat{\boldsymbol{e}}$). I_{J_c} is the energy of the corresponding ionization threshold ($I_{3/2}$ for $2p^5 3d$ and $I_{1/2}$ for $2p^5 3d'$).

The polarization vectors of the synchrotron light and the Ti:sapphire laser are parallel, and we choose our quantization (z) axis along this direction. Since the total angular momentum of the initial (ground) state is $J_i = 0$ and therefore $M_i = 0$, the accessible intermediate states have $J_\nu = 1$ and $M_\nu = 0$, and the nonzero dipole transition amplitudes $\langle \epsilon; \gamma M | D | \nu\rangle$ [see Eqs. (4) and (6)] have $M = 0$ and $J = 0$ or $J = 2$. By writing the final state in the form given by Eq. (4), we assume that the angular momentum J_c of the final state is well defined. Furthermore, we consider only those transitions between the intermediate states and the final state for which J_c remains unchanged. In the following we therefore omit explicit dependence of the dipole matrix elements and quantum defects on J_c.

The kinetic energy of the photoelectron measured in the present experiment lies in the energy range up to about 70 meV. The quantities of relevance for the calculation of the differential cross section—the quantum defects and the dipole matrix elements pertaining to various channels—can thus be obtained by extrapolation across the ionization thresholds. The quantum defects μ_γ attributed to the components of the continuum wave function in Eq. (4) have been obtained by means of

$$E_\gamma = I_{J_c} + \epsilon_\gamma = I_{J_c} - \frac{1}{2(n - \mu_{\gamma,n})^2} \quad (\text{for } \epsilon_\gamma < 0), \quad (7)$$

by extrapolating the values of μ_γ into the continuum ($\epsilon_\gamma \geqslant 0$). The exact energies of the ground and $2p^5 nl$ ($l = p, f$) excited states converging to both ionization thresholds have been taken from the NIST database [31]. In addition, bound-bound dipole matrix elements for the transitions to the aforementioned $2p^5 nl$ states have been calculated with GRASP Dirac-Fock codes [32]. The oscillator strength distribution has been extrapolated from the discrete part of the spectrum across the thresholds [33], and the values of the transition matrix elements have been determined from the extrapolated values. The resonances in the autoionization region have been treated as purely bound in the extrapolation procedure.

The states used in the extrapolation are characterized by the quantum numbers J_c, l, K, and J, and we therefore assign these quantum numbers to the extrapolated quantum defects and transition matrix elements. We treat these phase shifts $\pi\mu_\gamma$ as the Lu-Fano eigenphase shifts [34–36]. In the description introduced by Lu and Fano, the radial space is divided into the inner region and the asymptotic (outer) region in which the potential felt by an electron is only the screened Coulomb potential. The wave function is then written in terms of close-coupling channel functions used to describe the effects of the short-range electron correlations in the inner region, and in terms of collision channel functions which are used to describe the $Ne^+ + e^-$ complex in the asymptotic region. These two types of channel functions are connected through a unitary transformation.

In our case, we treat both the inner and outer region using the jK-coupling scheme, and no transformation between the functions describing the inner and outer region is needed. It should be noted here again that the closed channels—which are used to take into account the admixture of discrete components of the resonance wave functions in the autoionization region—have not been included in the description of the continuum

TABLE I. The symmetry of the final states used in the extrapolation ($n \to \epsilon$) of the quantum defects and the oscillator strengths across the ionization thresholds. Tabulated are the designations for the dipole transition amplitudes ($D_{Jl,a}$ or $D_{Jl,b}$ for $J_c = 3/2$; $\bar{D}_{Jl,a}$ or $\bar{D}_{Jl,b}$ for $J_c = 1/2$) and quantum defects ($\mu_{Jl,a}$ or $\mu_{Jl,b}$ for $J_c = 3/2$; $\bar{\mu}_{Jl,a}$ or $\bar{\mu}_{Jl,b}$ for $J_c = 1/2$).

Channel	$2p^5(^2P_{J_c})\,nl\,[K]_J$	Amplitude	Quantum defect
$\mathcal{A}$	$2p^5(^2P_{3/2})\,np\,[5/2]_2$	$D_{2p,a}$	$\mu_{2p,a}$
$\mathcal{B}$	$2p^5(^2P_{3/2})\,np\,[3/2]_2$	$D_{2p,b}$	$\mu_{2p,b}$
$\mathcal{C}$	$2p^5(^2P_{3/2})\,np\,[1/2]_0$	$D_{0p,a}$	$\mu_{0p,a}$
$\mathcal{D}$	$2p^5(^2P_{1/2})\,np\,[3/2]_2$	$\bar{D}_{2p,a}$	$\bar{\mu}_{2p,a}$
$\mathcal{E}$	$2p^5(^2P_{1/2})\,np\,[1/2]_0$	$\bar{D}_{0p,a}$	$\bar{\mu}_{0p,a}$
$\mathcal{F}$	$2p^5(^2P_{3/2})\,nf\,[3/2]_2$	$D_{2f,a}$	$\mu_{2f,a}$
$\mathcal{G}$	$2p^5(^2P_{3/2})\,nf\,[5/2]_2$	$D_{2f,b}$	$\mu_{2f,b}$
$\mathcal{H}$	$2p^5(^2P_{1/2})\,nf\,[5/2]_2$	$\bar{D}_{2f,a}$	$\bar{\mu}_{2f,a}$

wave function because the photon energy ω_L is tuned to avoid the resonances and since these resonances are very narrow. Therefore, this situation corresponds to the case of the Lu-Fano approach where all the considered channels are open (see Ref. [35] for details).

By rearranging Eq. (6), it can be shown that

$$\sum_{M_c,m_s} |\langle \boldsymbol{k}; J_c M_c m_s | D | \nu \rangle|^2 = \sum_{q=0}^{2} A_{2q} P_{2q}(\cos\theta). \tag{8}$$

Note that Eq. (8) follows directly from Eq. (6), where it is assumed that the dipole approximation is valid also in the second step of the two-photon process. Indeed, it has been checked that this assumption is reasonable: The lowest electric dipole (E1) oscillator strengths—in our case associated with the transitions to the $2p^5np$ Rydberg states used in the extrapolation procedure—are more than an order of magnitude larger than the highest electric quadrupole (E2) oscillator strengths to the $2p^5ng$ states.

The asymmetry parameters can thus be written as quotients:

$$\beta_2 = A_2/A_0 \quad \text{and} \quad \beta_4 = A_4/A_0. \tag{9}$$

We express these quotients in terms of the dipole transition amplitudes and quantum defects pertaining to the various final-state channels. The amplitudes and the quantum defects are characterized by the coupling of the core J_c, the orbital angular momentum l, and the total momentum J. In the following, the quantities pertaining to the $J_c = 1/2$ core will be denoted with a bar, so that they differ from the analogous quantities associated with the $J_c = 3/2$ core. Furthermore, an additional label $w = a,b$ will used to distinguish the channels with equal J_c and l, but with different values of the resultant K. The channels considered in the calculation and the corresponding transition amplitudes $D_{Jl,w}$ ($\bar{D}_{Jl,w}$) and quantum defects $\mu_{Jl,w}$ ($\bar{\mu}_{Jl,w}$) are listed in Table I.

The coefficients A_{2q} can be written in the form ($J, J' = 0,2$, $l,l' = p,f$, $w,w' = a,b$):

$$\bar{Q}_{Jlw,J'l'w'} = \bar{D}_{Jl,w}\bar{D}_{J'l',w'}\cos(\pi\bar{\mu}_{Jl,w} - \pi\bar{\mu}_{J'l',w'} + \sigma_l - \sigma_{l'}) \tag{10}$$

for $J_c = 1/2$ and

$$Q_{Jlw,J'l'w'} = D_{Jl,w}D_{J'l',w'}\cos(\pi\mu_{Jl,w} - \pi\mu_{J'l',w'} + \sigma_l - \sigma_{l'}) \tag{11}$$

for $J_c = 3/2$. Henceforth, we will use a single letter (the channel designation given in Table I) to denote the indices J,l,w and J',l',w'. For the core coupled to $J_c = 1/2$, the coefficients are

$$A_0 = \frac{1}{\pi k}\frac{1}{4}(\bar{Q}_{\mathcal{DD}} + \bar{Q}_{\mathcal{EE}} + \bar{Q}_{\mathcal{HH}}), \tag{12}$$

$$A_2 = \frac{1}{\pi k}\left(\frac{1}{4}\bar{Q}_{\mathcal{DD}} + \frac{\sqrt{2}}{2}\bar{Q}_{\mathcal{DE}} - \frac{\sqrt{6}}{14}\bar{Q}_{\mathcal{DH}} - \frac{\sqrt{3}}{2}\bar{Q}_{\mathcal{EH}} + \frac{2}{7}\bar{Q}_{\mathcal{HH}}\right), \tag{13}$$

$$A_4 = \frac{1}{\pi k}\left(\frac{3}{14}\bar{Q}_{\mathcal{HH}} - \frac{3\sqrt{6}}{7}\bar{Q}_{\mathcal{DH}}\right), \tag{14}$$

whereas for $J_c = 3/2$, we obtain

$$A_0 = \frac{1}{\pi k}\frac{1}{4}(Q_{\mathcal{AA}} + Q_{\mathcal{BB}} + Q_{\mathcal{CC}} + Q_{\mathcal{FF}} + Q_{\mathcal{GG}}), \tag{15}$$

$$A_2 = \frac{1}{\pi k}\left(\frac{1}{5}Q_{\mathcal{AA}} + \frac{3}{10}Q_{\mathcal{AB}} - \frac{3\sqrt{5}}{10}Q_{\mathcal{AC}} + \frac{3}{70}Q_{\mathcal{AF}} + \frac{3\sqrt{6}}{35}Q_{\mathcal{AG}} - \frac{1}{5}Q_{\mathcal{BB}} - \frac{\sqrt{5}}{10}Q_{\mathcal{BC}} + \frac{3}{10}Q_{\mathcal{BF}} - \frac{4\sqrt{6}}{35}Q_{\mathcal{BG}} - \frac{3\sqrt{5}}{10}Q_{\mathcal{CF}} - \frac{\sqrt{30}}{10}Q_{\mathcal{CG}} + \frac{1}{5}Q_{\mathcal{FF}} + \frac{3\sqrt{6}}{35}Q_{\mathcal{FG}} + \frac{11}{70}Q_{\mathcal{GG}}\right), \tag{16}$$

$$A_4 = \frac{1}{\pi k}\left(\frac{6}{7}Q_{\mathcal{AF}} + \frac{3\sqrt{6}}{14}Q_{\mathcal{AG}} + \frac{3\sqrt{6}}{14}Q_{\mathcal{BG}} + \frac{3\sqrt{6}}{14}Q_{\mathcal{FG}} - \frac{3}{28}Q_{\mathcal{GG}}\right). \tag{17}$$

Results of the theoretical treatment presented here will be discussed in Sec. IV. In particular, Figs. 4 and 5 in Sec. IV B present the calculated quantum defects and wave magnitudes as a function of kinetic energy of the electrons.

In contrast to the theoretical approach employed by Hotop *et al.* [15–17], we prefer the description of the continuum in terms of the jK-coupled channel functions to the description with the jj-coupled channel functions. Although, according to our calculations, the weights of the leading configuration state functions (CSFs) of the $2p^5np$ and $2p^5nf$ states are relatively high using the jj coupling scheme ($\gtrsim 90\%$), these states are almost pure in jK coupling (the weights of the leading CSFs being above 96% for $n \geqslant 4$). Since the extrapolation procedure is used to determine the phase shifts and dipole transition amplitudes (these are characterized by J_c, l, K, and J), it seems more natural to retain this description also for the continuum channels. It is possible to provide a link between the description of the continuum states used in this work with that considered in the work of Hotop *et al.* if one considers

that the final continuum state can also be expressed in terms of the jj-coupled channel functions:

$$|\boldsymbol{k};J_cM_cm_s\rangle = \sum_{l,m_l}\sum_{j}\sum_{J,M} i^l e^{-i\sigma_l} k^{-1/2} Y^*_{l,m_l}(\hat{\boldsymbol{k}}) \times \sum_{K,Q}(J_cM_c l m_l|KQ) \times (KQsm_s|JM)U_{b\gamma}|\epsilon;bM\rangle. \quad (18)$$

In Eq. (18), b denotes the quantum numbers J_c,l,j, and J, while γ denotes the quantum numbers in the jK-coupling scheme. The coupling considered in this case is $\boldsymbol{j}=\boldsymbol{l}+\boldsymbol{s}, \boldsymbol{J}=\boldsymbol{J}_c+\boldsymbol{j}$. As before, J_c and J are used for the angular momentum of the atomic core and for the total angular momentum, whereas l and j are the orbital and the total angular momentum associated with the continuum electron, respectively. The transformation matrix $U_{b\gamma}$ connecting the inner and outer region contains recoupling coefficients for the transformation between the jj and jK-coupling schemes:

$$U_{b\gamma} = (-1)^{J_c+l+s+J}\sqrt{2K+1}\sqrt{2j+1}\begin{Bmatrix} K & s & J \\ j & J_c & l \end{Bmatrix}. \quad (19)$$

We have used the equality,

$$e^{-i\pi\mu_\gamma}|\epsilon;\gamma M\rangle = \sum_j U_{b\gamma}|\epsilon;bM\rangle, \quad (20)$$

which holds for the case where all the considered channels are open [35].

B. Simplified model using reduced matrix elements

In the theoretical treatment of the photoionization process presented earlier, there are five open channels (limits $n\to\epsilon$ of $\mathcal{A}$, $\mathcal{B}$, $\mathcal{C}$, $\mathcal{F}$, and $\mathcal{G}$; see Table I) describing the $2p^53d \to 2p^5(^2P_{3/2})\epsilon p,\epsilon f$ ionization, and there are three channels ($\mathcal{D}$, $\mathcal{E}$, and $\mathcal{H}$) describing the $2p^53d' \to 2p^5(^2P_{1/2})\epsilon p,\epsilon f$ ionization. We assume in both cases that the photoionization with a change in J_c is negligible. In order to be able to completely characterize these channels, it would be necessary to have access to nine and five experimental parameters, respectively, even not counting the absolute cross section. In the experiments performed here, it is not possible to extract such a large number of parameters, and therefore some approximation is necessary in order to be able to extract the transition amplitudes and phase differences from the experimental results. Possible approximations in the description of the photoionization process will be implemented in this section, and their validity will be discussed in Sec. IV.

A commonly applied approximation (e.g., see Refs. [15–17]) is to neglect the spin-orbit interaction in the continuum and to assume that the orbital shapes and the phase differences do not depend on the total angular momentum (J) associated with the continuum channels. In order to derive simplified versions of the expressions for β_2 and β_4, we first transform the dipole matrix elements connecting the intermediate state $|\nu\rangle$ to the partial waves of the continuum wave function from jK coupling to jj coupling, and then successively apply the uncoupling formula [27]. For the present case, we obtain

$$\mathfrak{D}^{\nu}_{JlK}(\epsilon) = e^{i(\sigma_l+\pi\mu_l)}\langle\epsilon;[(J_c,l)K,s]JM|D|n_\nu;[(J_c,l_\nu)K_\nu,s]J_\nu M\rangle \quad (21a)$$

$$= (-1)^{J-M}\begin{pmatrix} J & 1 & J_\nu \\ -M & 0 & M \end{pmatrix}\hat{K}\hat{K}_\nu\hat{J}\hat{J}_\nu \times \sum_{j,j_\nu}\hat{j}^2\hat{j}_\nu^2(-1)^{3J_c+s+l_\nu+J_\nu}\begin{Bmatrix} K & s & J \\ j & J_c & l \end{Bmatrix} \times \begin{Bmatrix} K_\nu & s & J_\nu \\ j_\nu & J_c & l_\nu \end{Bmatrix}\begin{Bmatrix} J_c & j & J \\ 1 & J_\nu & j_\nu \end{Bmatrix}\begin{Bmatrix} l & s & j \\ j_\nu & 1 & l_\nu \end{Bmatrix} \times e^{i(\sigma_l+\pi\mu_l)}\langle\epsilon l\|\mathfrak{d}\|n_\nu l_\nu\rangle. \quad (21b)$$

The total (orbital + spin) angular momentum of the ϵl and the $3d$ electron are denoted by j and j_ν, respectively, and the notation $\hat{q}=(2q+1)^{1/2}$ has been introduced. The reduced single-electron dipole matrix element is denoted by $\langle\epsilon l\|\mathfrak{d}\|n_\nu l_\nu\rangle = \langle\epsilon l\|rC^1\|n_\nu l_\nu\rangle$, where $C^1_q(\hat{\boldsymbol{r}})=\sqrt{4\pi/3}Y_{1q}(\hat{\boldsymbol{r}})$ is the reduced spherical harmonic function. We took into account that J and J_ν are integers and that j and j_ν are half-integers. It should be noted that the dipole matrix element $\mathfrak{D}^{\nu}_{JlK}$ contains the phase factor and that the reduced matrix elements $\langle\epsilon l\|\mathfrak{d}\|n_\nu l_\nu\rangle$ and the total phase shifts $\sigma_l+\pi\mu_l$ are independent of j, J, j_ν, and J_ν. Note also that the dipole matrix element on the right-hand side of Eq. (21a) represents one of the transition amplitudes $D_{Jl,w}$ or $\bar{D}_{Jl,w}$. We can now express β_2 and β_4 with the quantities:

$$\left.\begin{aligned}\bar{R} &= \bar{D}_p/\bar{D}_f,\\ \bar{\Delta} &= \sigma_p-\sigma_f+\pi\bar{\mu}_p-\pi\bar{\mu}_f\end{aligned}\right\} J_c=1/2, \quad (22)$$

$$\left.\begin{aligned}R &= D_p/D_f\\ \Delta &= \sigma_p-\sigma_f+\pi\mu_p-\mu_f\end{aligned}\right\} J_c=3/2, \quad (23)$$

where the single-electron reduced matrix elements associated with the ϵp, $\epsilon p'$, ϵf, and $\epsilon f'$ continuum orbitals are $D_p=\langle\epsilon p\|\mathfrak{d}\|3d\rangle$, $\bar{D}_p=\langle\epsilon p'\|\mathfrak{d}\|3d'\rangle$, $D_f=\langle\epsilon f\|\mathfrak{d}\|3d\rangle$, and $\bar{D}_f=\langle\epsilon f'\|\mathfrak{d}\|3d'\rangle$, respectively. For $J_c=1/2$, we obtain

$$\beta_2 = \frac{49\bar{R}^2+144\sqrt{6}\bar{R}\cos\bar{\Delta}+96}{119\bar{R}^2+84}, \quad (24)$$

$$\beta_4 = \frac{24\sqrt{6}\bar{R}\cos\bar{\Delta}+72}{119\bar{R}^2+84}, \quad (25)$$

while for $J_c=3/2$, the result is

$$\beta_2 = \frac{R^2+4+6\sqrt{6}R\cos\Delta}{5(R^2+1)}, \quad (26)$$

$$\beta_4 = 0. \quad (27)$$

These approximations have also been applied within the general formalism introduced by Baier *et al.* [18] to describe the angular distribution of photoelectrons generated from the photoionization of aligned intermediate states. We will briefly discuss this formalism as it both validates the theoretical framework applied here and provides easy comparison to results obtained using other experimental geometries. The formalism of Baier *et al.* [18], which is very similar to the

formalism of Cherepkov *et al.* [19], provides a generalized treatment of the photoionization of aligned atoms as it conveniently separates the contributions of the polarization of the intermediate state, the dynamics of the photoionization process, and the geometry of the experiment. Indeed the angular distribution of photoelectrons is given by

$$\frac{d\sigma}{d\Omega} = \frac{\sigma^{(\mathrm{iso})}}{4\pi}\left[1 + \sum_{k_0,k,k_\gamma} \bar{A}_{k_0 0}\beta_{k_0 k k_\gamma} F_{k_0 k k_\gamma}\right], \qquad (28)$$

where $\sigma^{(\mathrm{iso})}$ is the integral cross section for the photoionization of unpolarized atoms, $\bar{A}_{k_0 0}$ are the reduced statistical tensors which describe the alignment of the intermediate state, $\beta_{k_0 k k_\gamma}$ are the dynamical parameters which contain the information on the photoionization process, and $F_{k_0 k k_\gamma}$ are the kinematic parameters which describe the experimental geometry and the polarization state of the photons of the ionizing radiation.

The expressions for the dynamical parameters $\beta_{k_0 k k_\gamma}$ are written in terms of reduced matrix elements $\langle \xi J_c l j J \| D \| \xi_v J_v \rangle$ and their complex conjugates, where ξ and ξ_v represent additional quantum numbers of the final and intermediate states. These matrix elements can also be expressed in terms of the reduced matrix elements D_p and D_f ($\bar{D}_p$ and $\bar{D}_f$). Indeed, this has recently been done (see Eq. (13) of Ref. [13]) by means of an expression analogous to Eq. (21b) for the case where the final state is written using jj coupling.

The subsequent step involves summation over all possible values of j and J, which is equivalent to the summation over K and J in Eq. (4). This leads to an expression for the $\beta_{k_0 k k_\gamma}$ parameters in terms of the reduced matrix elements [see Eq. (15) of Ref. [13]]. We have used this approach, together with the suitable expressions for the geometrical parameters $F_{k_0 k k_\gamma}$ for our geometry, and the values of $\bar{A}_{00} = 1$ and $\bar{A}_{20} = -\sqrt{2}$ for the alignment of the intermediate state in our geometry, to describe the PADs measured in our experiments. Comparing the expression obtained in this way to the expression for the angular distributions in terms of β_2 and β_4 allows us to again derive the expressions for β_2 and β_4 in terms of the reduced matrix elements and the phase differences of the outgoing waves. As expected, implementing this procedure for the intermediate states probed here reproduces Eqs. (24)–(27), thus, in the limit of the assumptions used in the present section, validating the theoretical description outlined in Sec. III A.

IV. RESULTS AND DISCUSSION

The PADs of the electrons emitted in the processes (3) and (2) have been measured at several fixed energies above the respective ionization thresholds. A subset of the velocity map images is shown in Fig. 2, where the raw data are shown on the top half of each map and the inverted image using pBasex [28] is shown in the bottom halves. The inversion process involves the use of basis set functions of the form of Eq. (1) and thus it is intrinsically assumed that the PAD has this form. The β_2 and β_4 parameters extracted from the entire data set of images are listed in Tables II and III, where they are compared to the values obtained using the theoretical framework of Sec. III A. These results will be discussed further in Sec. IV B.

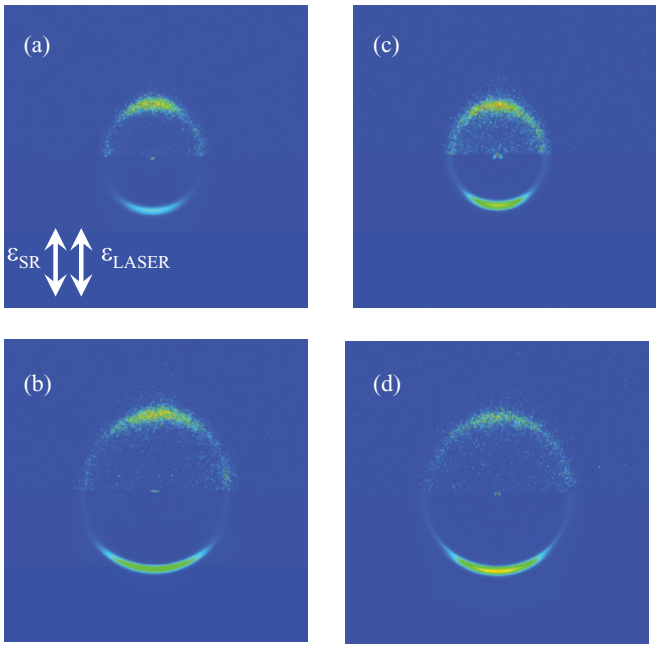

FIG. 2. (Color online) Photoelectron velocity map images for the $2p^5(^2P_{1/2})3d[3/2]_1 \rightarrow 2p^5(^2P_{1/2})\epsilon p,\epsilon f$ excitation recorded at (a) 23 meV and (b) 47 meV above the ionization threshold, and images of the $2p^5(^2P_{3/2})3d[3/2]_1 \rightarrow 2p^5(^2P_{3/2})\epsilon p,\epsilon f$ excitation at (c) 20 meV and (d) 45 meV above the threshold. The upper part of each map contains the raw image, while the lower part shows the pBasex inverted image. The polarization of the synchrotron and the polarization of the laser are shown in (a).

The calculated and measured asymmetry parameters are shown in Fig. 3. One point to note here is that β_2 and β_4 vary smoothly (see Table III) also in the autoionization region due to the suitably chosen energies of the Ti:sapphire laser. For the lower two energy points (which lie in the energy region where the energy spacing between the resonances is relatively large) it has been easy to avoid the double resonance excitation by suitably tuning the laser. For the higher kinetic energy value, where the spacing between the $2p^5nf$ resonances is of the order of 2 meV, it was feared that the higher density of Rydberg states would strongly perturb the PADs. However, this does not appear to be the case. Furthermore, the $2p^5np$ which are interspersed between the $2p^5nf$ resonances are approximately two orders magnitude weaker than the nf resonances.

TABLE II. Experimental and theoretical asymmetry parameters for the $2p^5(^2P_{1/2})3d[3/2]_1 \rightarrow 2p^5(^2P_{1/2})\epsilon p,\epsilon f$ excitation.

	Experiment		Theory	
ϵ (meV)	β_2	β_4	β_2	β_4
13	1.07 ± 0.06	0.81 ± 0.04	0.949	0.817
23	1.11 ± 0.07	0.87 ± 0.06	0.958	0.818
33	1.15 ± 0.08	0.81 ± 0.06	0.965	0.819
47	1.27 ± 0.06	0.94 ± 0.06	0.975	0.821
72	1.27 ± 0.06	0.92 ± 0.04	0.985	0.822

TABLE III. Experimental and theoretical asymmetry parameters for the $2p^5(^2P_{3/2})3d[3/2]_1 \rightarrow 2p^5(^2P_{3/2})\epsilon p,\epsilon f$ excitation.

	Experiment		Theory	
ϵ (meV)	β_2	β_4	β_2	β_4
20	0.84 ± 0.12	0.42 ± 0.04	0.843	0.348
45	0.87 ± 0.06	0.40 ± 0.04	0.867	0.350
70	0.93 ± 0.16	0.39 ± 0.08	0.880	0.352

A. Analysis of the angular distributions using simplified model

As outlined in Sec. III B, a common approach used to reduce the number of independent parameters needed to describe the photoionization process is to neglect the spin-orbit interaction in the continuum and to assume that the continuum orbitals and phase shifts do not depend on the quantum numbers associated with various p and various f channels. In the case of ionization

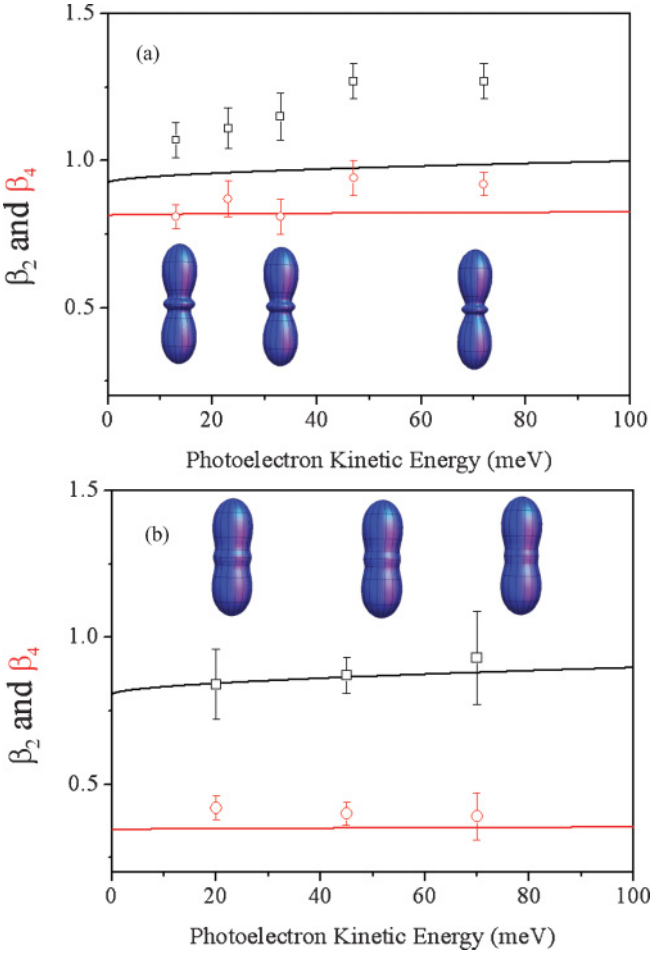

FIG. 3. (Color online) The theoretical and experimental asymmetry parameters β_2 (open squares) and β_4 (open circles) for the photoionization of the (a) Ne $2p^5(^2P_{1/2})3d[3/2]_1$ and (b) Ne $2p^5(^2P_{3/2})3d[3/2]_1$ states. The experimental values are extracted from the PADs, whereas the theoretical values (solid lines) were obtained using the quantum defect treatment outlined in Sec. III A. The angular distributions are depicted graphically as surfaces in the insets where the distance from the origin to the surface is proportional to the probability that the electron is emitted in that direction.

TABLE IV. Experimentally determined ratios of the radial dipole matrix elements and cosine of their phase differences for the $2p^5(^2P_{1/2})3d^2[3/2]_1 \rightarrow 2p^5(^2P_{1/2})\epsilon l$ $(l = p, f)$. The kinetic energy of the emitted electrons is denoted by ϵ.

ϵ (meV)	$\bar{R}$	$\cos\bar{\Delta}$
13	$0.19^{+0.11}_{-0.19}$	$0.03^{+0.10}_{-0.03}$
23	$0.13^{+0.12}_{-0.12}$	$0.01^{+0.03}_{-0.01}$
33	$0.22^{+0.15}_{-0.21}$	$-0.05^{+0.05}_{-0.11}$
47	$0.05^{+0.10}_{-0.03}$	$-0.004^{+0.004}_{-0.006}$
72	$0.05^{+0.10}_{-0.03}$	$-0.007^{+0.007}_{-0.003}$

of the $2p^5 3d'$ intermediate state, this procedure reduces the number of parameters describing the ionization process to the number of experimentally accessible parameters. In other words, Eqs. (24) and (25) represent a set of two equations with two unknowns, and can therefore be inverted to give

$$\bar{R} = \frac{2\sqrt{3}\sqrt{-4-\beta_2+6\beta_4}}{\sqrt{-7+17\beta_2-102\beta_4}}, \tag{29}$$

$$\cos\bar{\Delta} = \frac{14\bar{R}-34\beta_2+29\beta_4\bar{R}}{-32\sqrt{6}-8\sqrt{6}\beta_2+8\sqrt{6}\beta_4}. \tag{30}$$

Using these equations, it is now possible to extract the ratio $\bar{R}$ and the cosine of the phase difference $\cos\bar{\Delta}$. These extracted values are listed in Table IV. The uncertainties have been extracted by numerical propagation of the errors through Eqs. (29) and (30) and taking only real values to form the new error limits.

The overall conclusion is that the dominant outgoing wave is an ϵf wave, which appears to increase in relative intensity as the kinetic energy ϵ increases. Furthermore, it appears that the phase difference goes through a $\pi/2$ value in the energy region of interest. However, the quite large uncertainties resulting from the error propagation hamper definitive conclusions.

The case is less clear for the $J_c = 3/2$ core, where it can be seen from Eq. (27) that the β_4 parameter is predicted to be zero within the approximations outlined in Sec. III B. Clearly, in this case, it is not possible to invert the equations and to extract the values of R and $\cos\Delta$ as there is only a single equation with two unknowns. Moreover, the measured values of β_4 point to a breakdown of the theoretical model used to describe the photoionization process (see Table III). This indicates that at least one of the simplifying assumptions made does not hold. The identification of which of the assumptions does not hold will be investigated in the following section.

B. Analysis of the angular distributions using the quantum defect theory

In the derivation of Eqs. (24)–(27), which connect the asymmetry parameters to the partial-wave amplitudes and phase differences, a number of approximations are made. Some of them lead to incorrect results for the case of the $J_c = 3/2$ core. On the other hand, the more general approach of Sec. III A, in which no simplifying assumptions are made about the dependence of the dipole matrix elements and phase shifts on the channel quantum numbers, provides good agreement

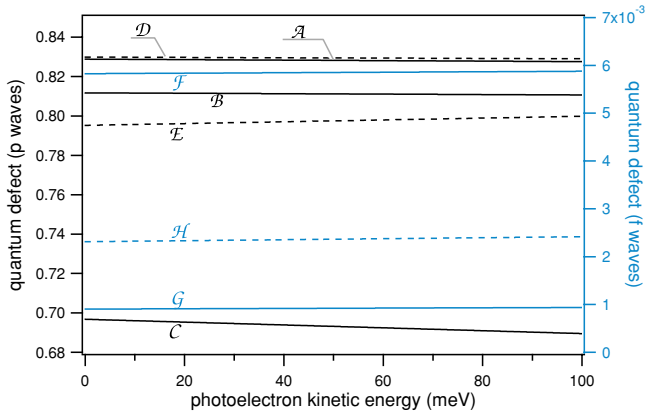

FIG. 4. (Color online) The extrapolated quantum defects of $2p^5\epsilon p$ (left axis) $2p^5\epsilon f$ (right axis) waves. The results for $J_c = 1/2$ and $J_c = 3/2$ core are plotted with dashed and solid lines, respectively. The labels $\mathcal{A}$–$\mathcal{H}$ indicate the channels given in Table I.

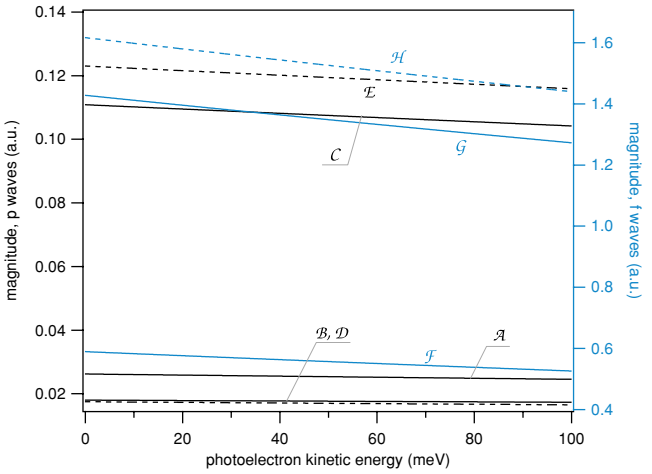

FIG. 5. (Color online) The magnitude of the p wave (left axis) and the f wave (right axis) extrapolated dipole transition amplitudes. Given are $\sqrt{\omega_L}|D_{Jl,w}|$ and $\sqrt{\omega_L}|\bar{D}_{Jl,w}|$ of the channels from Table I. The matrix elements for the $J_c = 1/2$ and $J_c = 3/2$ core are plotted with dashed and solid lines, respectively.

with the values of β_2 and β_4 obtained experimentally for photoionization of both intermediate states probed in this work.

This agreement is shown in Fig. 3, and the values obtained through the extrapolation procedure for different values of the photoelectron kinetic energy ϵ are listed in Tables II and III. In particular, β_4, which is constrained to zero when the single-electron matrix elements and the phase differences are assumed to be independent of j and J, is now in good agreement with the measured values. This clearly indicates that the assumptions made are not valid for the ejection of the electron into the continuum at least in the $J_c = 3/2$ case. Although the spin-orbit coupling in the continuum is weak, the dependence of the dipole transition amplitudes and phase shifts on the quantum numbers describing various channels of the continuum wave function must be retained.

The quantum defects $\mu_{Jl,w}$ and $\bar{\mu}_{Jl,w}$ and the magnitudes $\sqrt{\omega_L}|D_{Jl,w}|$ and $\sqrt{\omega_L}|\bar{D}_{Jl,w}|$ of the matrix elements obtained with extrapolation are shown in Figs. 4 and 5. The extrapolated dipole transition amplitudes show that the f-wave channels are dominant for both couplings of the core, as can be seen from Fig. 5. This result is consistent with Sec. IV A. As can be seen, for both $J_c = 1/2$ and $J_c = 3/2$, the dominant contribution to the cross section stems from the $J = 2$, $K = 5/2$ f-wave channel ($\mathcal{G}$ and $\mathcal{H}$). Furthermore, the largest contribution stemming from the p-wave channels is $J = 0$, $K = 1/2$ ($\mathcal{C}$ and $\mathcal{E}$) for both core couplings.

From Figs. 4 and 5 it seems that channel-dependent dipole matrix elements are necessary for the correct description of the PADs. In order to check the role of the channel dependence of the quantum defects, we performed a quick proof-of-principle calculation with fixed values of $\mu_p = \bar{\mu}_p = 0.8$ and $\mu_f = \bar{\mu}_f = 6 \times 10^{-3}$, but with channel-dependent dipole matrix elements $D_{Jl,w}$ and $\bar{D}_{Jl,w}$. This yields approximately correct β_2 and β_4 values; in particular, it gives $\beta_4 \approx 0.35$ also for the case of the $J_c = 3/2$ core. The latter result indicates that the channel-dependent matrix elements are indeed needed for the correct description of the PADs in the present geometry. This means that according to the present quantum defect treatment it is the assumptions made about the single-electron dipole matrix elements in Sec. IV A which result in the incorrect β_4 value for the case of the $J_c = 3/2$ coupling of the $2p$ electrons.

C. Comparison with other experimental geometries

In experiments combining synchrotron and laser radiation, the most commonly used electron analyzers are hemispherical (e.g., Refs. [13,37]) and cylindrical mirror analyzers (e.g., Refs. [38,39]). Indeed, these types of analyzers are particularly suitable for detecting electrons with kinetic energy in the range of 5–1000 eV. As a consequence, they are perfectly suited to experiments in which the laser light is used to excite the target and the synchrotron radiation is used to ionize the inner shell of the resulting polarized target (e.g., Refs. [37–39]) since the resulting electrons have favorable kinetic energies for detection by such analyzers. The situation is significantly less favorable when the laser is used as the ionizing source because the resulting electrons typically have very low kinetic energy. Nonetheless, the hemispherical analyzer has been used to detect photoelectrons from Ar atoms aligned by excitation with synchrotron radiation [13]. The geometry adopted in that experiment is shown in Fig. 6, where it can be seen that the light sources propagate perpendicularly to each other, and the electrons are detected along an axis which is perpendicular to the direction of propagation of both the pump and probe light sources.

The "angular distribution" of the electrons is measured by keeping the electron detection axis fixed, but rotating the electric field vector of the ionizing radiation with respect to the detection axis. However, on examination of the geometrical parameters $F_{k_0kk_\gamma}$ introduced by Baier *et al.* [18] for this geometry it can be seen that this angular distribution only depends on terms containing $P_2(\cos\vartheta)$, where ϑ is the angle between the electric field vector of the ionizing laser radiation and the axis along which the electrons are detected, and therefore only a single experimental parameter can be

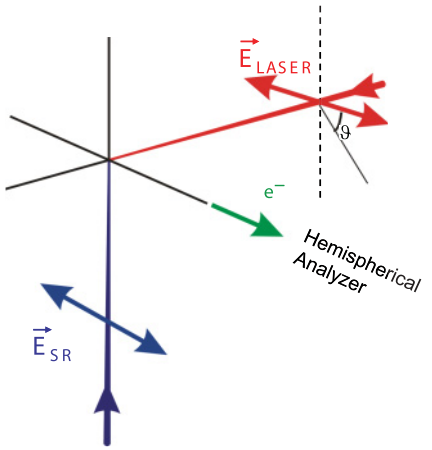

FIG. 6. (Color online) Schematic view of the geometry of the experimental setup used in Ref. [13]. In this case electrons are detected along a single axis and ϑ is the angle between the electric field vector of the laser radiation and this axis. See text for discussion.

extracted from the angular distributions measured in this way. In the geometry used here, the F_{242} geometrical term contains a dependence on the $P_4(\cos\theta)$ term (in this case, θ is the angle between the electric field vector of the ionizing light and the direction of emission of the photoelectron). As a result, two parameters (β_2 and β_4) can be extracted from each velocity map image.

Finally, it should be noted that the same parameters as those extracted using the velocity map imaging geometry are accessible using a hemispherical analyzer if either the polarizations of both the synchrotron radiation and laser are variable or if the detector axis can be rotated around the direction of propagation of the radiation sources (in a counterpropagating geometry). While both of these solutions are possible, the first is not very common at synchrotron radiation beam lines, while the second is often difficult to implement due to the large physical size of analyzers used at synchrotron beam lines. It should be noted that the second of these experiments has been performed in a synchrotron + laser setup for relatively fast electrons. In this case, the synchrotron was used as the ionization radiation (e.g., Ref. [40]). In comparison to the latter experimental approach, the velocity map imaging geometry retains the significant advantage that it has 4π solid angle detection, thus making also very weak signal detectable. One final point to be mentioned is that the VMI setup is limited to the detection of relatively low-energy electrons in comparison to traditional analyzers. For example, the highest kinetic energy electrons detected to date using is this method are about 40 eV although simulations suggest that electrons up to 100 eV will be accessible using this technique [41,42]. Nonetheless, this type of analyzer should be considered as complementary rather than an alternative to traditional analyzers.

V. CONCLUSIONS

In this work, we present an experimental and theoretical study of the angular distributions of photoelectrons ejected from the Ne $2p^5(^2P_{1/2})3d[3/2]_1$ and Ne $2p^5(^2P_{3/2})3d[3/2]_1$ states. These polarized intermediate states are prepared by photoexcitation using synchrotron radiation, and are subsequently ionized using linearly polarized light from a tunable Ti:sapphire laser. One of the innovative aspects of this work is that the angular distributions of the photoelectrons have been measured using the velocity map imaging technique, which has been combined with synchrotron radiation and laser experiments for the first time. The β_2 and β_4 asymmetry parameters extracted from the velocity map images are compared to the results of a quantum defect approach. If the description of the outgoing channels is simplified by introducing single-electron reduced dipole matrix elements in order to fully describe the ionization process in terms of only three parameters (the p-wave transition amplitude, the f-wave transition amplitude, and the phase difference between these waves), it is not possible to reproduce the measured β_4 values for the ionization of the Ne $2p^5(^2P_{3/2})3d[3/2]_1$ intermediate state. Good agreement is found only if dependence of the transition matrix elements on the channel quantum numbers of the continuum wave function is considered. Finally, the advantages of the velocity map imaging detection scheme for the measurement of the photoelectron angular distributions in pump-probe experiments is discussed over previously used methods. In particular, it is shown that the VMI geometry, which allows the extraction of β_2 and β_4 from the measured PADs, provides more information on the ionization process than geometries in which fixed one-dimensional (1D) detectors are used and only the polarization of the ionizing light is changed.

ACKNOWLEDGMENTS

The authors thank the Elettra support program for Italian users, and the staff of Elettra for providing high-quality light. E.O. thanks the ICTP-Elettra Users' Program. The authors also thank P. Lambropoulos for very fruitful discussions on the theoretical treatments outlined in this work. This research was partly supported by a Marie Curie Reintegration Grant within the 7th European Community Framework Programme.

[1] H. Klar and H. Kleinpoppen, J. Phys. B **15**, 933 (1982).
[2] F. J. Wuilleumier and M. Meyer, J. Phys. B **39**, R425 (2006).
[3] M. Meyer, Nucl. Instrum. Methods Phys. Res., Sect. A **601**, 88 (2009).
[4] A. N. Grum-Grzhimailo, E. V. Gryzlova, D. Cubaynes, E. Heinecke, M. Yalçinkaya, P. Zimmermann, and M. Meyer, J. Phys. B **42**, 171002 (2009).
[5] D. Cubaynes *et al.*, Phys. Rev. A **80**, 023410 (2009).
[6] J. Niskanen, S. Urpelainen, K. Jänkälä, J. Schulz, S. Heinäsmäki, S. Fritzsche, N. M. Kabachnik, S. Aksela, and H. Aksela, Phys. Rev. A **81**, 013406 (2010).
[7] A. Moise, M. Alagia, L. Avaldi, V. Feyer, K. C. Prince, and R. Richter, J. Phys. B **43**, 215001 (2010).
[8] M. Mizutani, M. Tokeshi, A. Hiraya, and K. Mitsuke, J. Synchrotron Radiat. **4**, 6 (1997).

[9] S. Aloïse, P. O'Keeffe, D. Cubaynes, M. Meyer, and A. N. Grum-Grzhimailo, Phys. Rev. Lett. **94**, 223002 (2005).
[10] I. D. Petrov, T. Peters, T. Halfmann, S. Alose, P. O'Keeffe, M. Meyer, V. L. Sukhorukov, and H. Hotop, Eur. Phys. J. D **40**, 181 (2006).
[11] Y.-Y. Lee *et al.*, Phys. Rev. A **78**, 022509 (2008).
[12] A. Moise, M. Alagia, L. Banchi, M. Ferianis, K. C. Prince, and R. Richter, Nucl. Instrum. Methods Phys. Res. A **588**, 502 (2008).
[13] K. Mitsuke, Y. Hikosaka, and K. Iwasaki, J. Phys. B **33**, 391 (2000).
[14] L. H. Haber, B. Doughty, and S. R. Leone, Phys. Rev. A **79**, 031401 (2009).
[15] A. Siegel, J. Ganz, W. Bussert, and H. Hotop, J. Phys. B **16**, 2945 (1983).
[16] S. Schohl, D. Klar, N. A. Cherepkov, I. D. Petrov, K. Ueda, S. Baier, R. Kau, and H. Hotop, J. Phys. B **30**, 609 (1997).
[17] S. Schohl, N. A. Cherepkov, I. D. Petrov, V. L. Sukhorukov, S. Baier, and H. Hotop, J. Phys. B **31**, 3363 (1998).
[18] S. Baier, A. N. Grum-Grzhimailo, and N. M. Kabachnik, J. Phys. B **27**, 3363 (1994).
[19] N. A. Cherepkov, V. V. Kuznetsov, and V. A. Verbitskii, J. Phys. B **28**, 1221 (1995).
[20] A. Verweyen, A. N. Grum-Grzhimailo, and N. M. Kabachnik, Phys. Rev. A **60**, 2076 (1999).
[21] R. R. Blyth *et al.*, J. Electron Spectrosc. Relat. Phenom. **101-103**, 959 (1999).
[22] G. M. Lawrence and H. S. Liszt, Phys. Rev. **178**, 122 (1969).
[23] W. F. Chan, G. Cooper, X. Guo, and C. E. Brion, Phys. Rev. A **45**, 1420 (1992).
[24] D. H. Parker and A. T. J. B. Eppink, J. Chem. Phys. **107**, 2357 (1997).
[25] G. Cautero, R. Sergo, L. Stebel, P. Lacovig, P. Pittana, M. Predonzani, and S. Carrato, Nucl. Instrum. Methods Phys. Res. A **595**, 447 (2008).
[26] P. O'Keeffe *et al.* (submitted to Rev. Sci. Instrum.).
[27] R. D. Cowan, *The Theory of Atomic Structure and Spectra* (University of California, Berkeley, 1981).
[28] G. A. Garcia, L. Nahon, and I. Powis, Rev. Sci. Instrum. **75**, 4989 (2004).
[29] C. Pan and A. F. Starace, Phys. Rev. A **44**, 324 (1991).
[30] P. Lambropoulos, P. Maragakis, and J. Zhang, Phys. Rep. **305**, 203 (1998).
[31] NIST Atomic Spectra Database [http://www.nist.gov/physlab/data/asd.cfm].
[32] K. G. Dyall, I. P. Grant, C. T. Johnson, F. A. Parpia, and E. P. Plummer, Comput. Phys. Commun. **55**, 425 (1989).
[33] U. Fano and J. W. Cooper, Rev. Mod. Phys. **40**, 441 (1968).
[34] U. Fano, Phys. Rev. A **2**, 353 (1970).
[35] K. T. Lu, Phys. Rev. A **4**, 579 (1971).
[36] C.-M. Lee and K. T. Lu, Phys. Rev. A **8**, 1241 (1973).
[37] D. Cubaynes *et al.*, Phys. Rev. Lett. **92**, 233002 (2004).
[38] J. M. Bizau, D. Cubaynes, P. Gerard, F. J. Wuilleumier, J. L. Picqué, D. L. Ederer, B. Carré, and G. Wendin, Phys. Rev. Lett. **57**, 306 (1986).
[39] M. Meyer, B. Müller, A. Nunnemann, T. Prescher, E. v. Raven, M. Richter, M. Schmidt, B. Sonntag, and P. Zimmermann, Phys. Rev. Lett. **59**, 2963 (1987).
[40] M. Pahler *et al.*, Phys. Rev. Lett. **68**, 2285 (1992).
[41] O. Ghafur, W. Siu, P. Johnsson, M. F. Kling, M. Drescher, and M. J. J. Vrakking, Rev. Sci. Instrum. **80**, 033110 (2009).
[42] P. Johnsson, W. Siu, A. Gijsbertsen, J. Verhoeven, A. S. Meijer, W. Van Der Zande, and M. J. J. Vrakking, J. Mod. Opt. **55**, 2693 (2008).